

Research on the characteristics of present crustal deformation in Beijing area based on GNSS

Y. Li^{1,2*}, Y. B. Wang², H. B. Shi², J. Zhu²

¹Institute of Geophysics, China Earthquake Administration, Beijing, China - yli@seis.ac.cn

²Department of Geophysical Network, China Earthquake Networks Center, China Earthquake Administration, Beijing, China - (yli, ybwang, hbshi, zhujie)@seis.ac.cn

Commission III, ICWG III/IVa

KEY WORDS: GNSS, Crustal deformation, Velocity field, Strain rate field, Active fault.

ABSTRACT:

We use the GAMIT/GLOBK software to process more than 100 GNSS sites observation covering the Beijing area from 1999-2021 to obtain the three-dimensional velocity field of present-day crustal movement, and the deformation and strain characteristics of Beijing were calculated and comprehensively analyzed by combining with historical earthquakes. The results show that: 1) The present-day horizontal crustal motion of Beijing is dominated by the SEE direction with a rate of 5-10 mm/a with relative to the stable Eurasian reference frame, and the northern and southern areas show uplift as a whole with a rate of 1-3 mm/a, while the central plain area shows overall subsidence, with a maximum subsidence rate of about 130 mm/a. 2) The horizontal deformation is mainly N-E/N-W extension, accompanied by weak shear activity. 3) The N-W trending faults show sinistral strike slip movement as a whole, with about 1.1-2.0 mm/a, and N-E trending faults show dextral strike slip with a rate of less than 1 mm/a. 4) The historical large earthquakes are distributed within the positive and negative gradient zones of the first shear strain rate, transition zones of the rotation rate, and are mostly distributed at the edges of the high and low value zones of the second shear strain rate, and the edges of the high value zones of the east-west strain rate also have a background of large earthquakes.

1. INTRODUCTION

Beijing is located at the intersection of Zhangjiakou-Bohai seismic zone, the North China Plain seismic zone and Fenwei seismic zone. It is an area with strong neotectonic activity, with complex geological tectonic environment and developed active faults (Ma, 1964; Gao et al., 1993). In modern seismic zoning, it is also located in the North China seismic area with strong seismic activity in the east of China (Gao, 2015). Since the historical records, 13 destructive earthquakes with $M \geq 5.0$ have occurred in this area, and the M8.0 earthquake named Sanhe-Pinggu happened in 1679 was the largest earthquake (Ren, 1996; Ran et al., 1997). It has been 292 years since the latest earthquake with $M \geq 6.0$ (happened in 1730). According to Qin Siqing's study on the recurrence cycle of the Beijing-Tianjin-Tangshan earthquake zone, the recurrence cycle of earthquakes with $M \geq 6$ in this region is about 280-300 years (<http://blog.sciencenet.cn/blog-575926-776449.html>), and therefore, from this perspective, there is a risk of future earthquakes in Beijing and the surrounding area.

Earthquake is a specific manifestation of crustal motion or tectonic deformation and the rapid release of elastic strain energy due to sudden destabilization of the source rock (Xu et al., 2002). The crustal deformation is caused by the accumulation of stress and strain, and tectonic earthquakes are accompanied by different degrees of crustal deformation throughout the process from conception, occurrence to post-seismic adjustment (Jiang et al., 2012). Since the availability of GNSS observations, many researchers at home and abroad have used GNSS data to conduct in-depth studies on regional crustal deformation and seismic activities, and have achieved fruitful

results (Jiang et al. 2003; Yang et al. 2001; Guo et al. 2007; Qiao et al., 2008; Wang and Shen, 2020).

In this paper, we calculate more than 100 GNSS sites observation covering the Beijing area, to obtain the three-dimensional velocity field of present-day crustal movement, and to analyze the deformation and strain characteristics of this region. Meanwhile, the activity of the main active faults in the domain was comprehensively examined with the regional historical earthquakes.

2. GNSS DATA PROCESSING

2.1 GNSS Data

In this paper, we collect and process GNSS data from multiple sources (listed and shown in Table 1 and Figure 1), which are described as follows: (a) 4 continuous and 42 campaign sites from the Crustal Motion Observation Network of China (CMONOC) project Phase-I/II. In each campaign session, 96 hours of data were collected per site. (b) 55 continuous sites shared from China Meteorological Administration (CMA). (c) 1 continuous site built and operated by National Institute of Metrology (NIM). The specific observation periods and sessions are shown in Table 1.

Type	Num	Attribution	Time span & Observation frequency
Continuous site	2	CMONOC-I	1998-2021
	2	CMONOC-II	2011-2021

* Corresponding author.
E-mail address: yli@seis.ac.cn

	55	CMA	2011-2021
	1	NIM	2008-2021
Campaign site	42	CMONOC-I/II	1999/2001/2004/2007/2009/2010/2011/2012/2013/2014/2015/2016/2017

Table 1. Data sources and observation frequency.

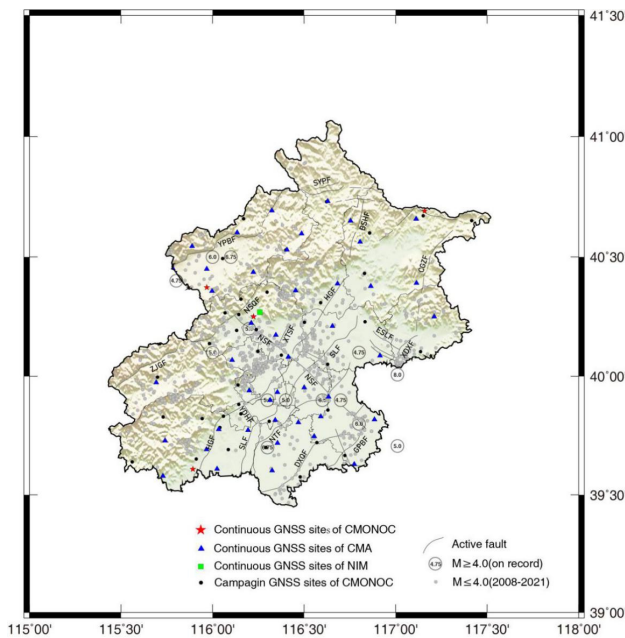


Figure 1. Tectonic setting and locations of GNSS sites of Beijing area.

Site shapes and colors represent data sources. Continuous and campaign sites are denoted by red star, blue triangle, green square and black circle, respectively. Thick and thin black solid lines are the administrative boundaries of Beijing and its districts respectively. Gray solid lines are the active faults, and the fault name abbreviations are as follows: ZJGF, Zijianguan Fault, NSQF, Nankoushanqian Fault, YPBF, Yanfanpendi Beiyuan Fault, SYPF, Shangyi-Pingquan Fault, NSF, Nankou-Sunhe Fault, SLF, Shunyi-Liangxiang Fault, NTF, Nanyuan-Tongxian Fault, HGF, Huangzhuang-Gaoliying Fault, YDHF, Yongdinghe Fault, BSHF, Beishicheng-Hefangkou Fault, GPBF, Guanpendi Beiyuan Fault, ESLF, Ershilichangshan Fault, CGZF, Chenggezhuang Fault, XDXF, Xiadianxin Fault. The gray dots represent the earthquake lower than M4.0 occurred between 2008 to 2021. The large hollow circles are the earthquake greater than M4.0 that have occurred on record, the number indicates the magnitude of the earthquake.

2.2 Data Processing

We use the GAMIT/GLOBK software package (Herring et al., 2010a, 2010b) to process all the raw GNSS data with a unified processing strategy, which will ensure the quality and self-consistency of all the solutions (Li, 2013). The major geophysical models and correction parameters used in data processing are listed in Table 2. (Boehm et al., 2006, 2007; Lagler et al., 2013; Lyard et al., 2006; Saastamoinen, 1973; Macmillan and Maus, 2005; Maus et al., 2005b). Instead of using the IGS precise orbits or daily solutions of global tracking sites from the IGS Analysis Centers, we process ~220 IGS sites distributed worldwide simultaneously to estimate the

Earth Orientation Parameters, (polar motion and ut1), satellite orbits, and site position parameters together. The advantage of this approach is that it can minimize the potential biases as comprehensively as possible, such as the ones led to by changes of geophysical models and parameters adopted in IGS orbit productions (Shen et al., 2011).

The GAMIT software adopts the double-difference approach to process the carrier-phase data, which limits the number of sites to be used in a single solution under a certain amount of computational power (Li, 2021). For the data observed before 2011, the number of stations observed per day is relatively smaller, all the campaign data are processed together with the global IGS data to obtain one daily solution directly. After 2012, the data are processed in more than one group divided by the regional site locations, with several continuous sites included in each of the campaign solutions. The daily solutions are loosely constrained, and the parameters on earth orientation, satellite orbits, and site positions are output along with their variance/covariance matrices. The regional daily solutions of the same day are combined with the global daily solutions to realize the Terrestrial Reference Frame ITRF2014 by using the GLOBK module based on Kalman filter method.

Elevation cutoff angle and data weighting	10° , data weighting depending on the elevation angle
Data sampling	30 s for data editing, and 120 s for parameter estimation
Antenna phase center (satellite and receiver)	IGS ANTEX files are used to correct absolute PCVs of satellite and receiver, satellite antenna offsets are estimated as parameters
Ionospheric refraction	Ionosphere-free linear combination
Troposphere refraction	Saastamoinen model (Saastamoinen, 1973) for dry delay and the piecewise-linear parameter estimation in 1 hour intervals for wet delays. The Liner troposphere horizontal gradients in 24-hour interval are estimated. Meteorologic elements and mapping function are based on the global model (GPT or GPT2) (Boehm et al., 2006, 2007; Lagler et al., 2013)
Ocean tide	FES2004 model (Lyard et al., 2006) with correction for the center-of-mass motion
Solid Earth tide, pole tide	Models recommended by IERS Conventions 2010 (http://www.iers.org/TN36)

Table 2. Major geophysical models and parameters used in GAMIT GNSS data processing.

3. CRUSTAL DEFORMATION RESULT

3.1 3-D Velocity Field

The main methods to obtain the secular velocity of GNSS sites are as follows: (1) Estimation only based on the site position time series. (2) Estimation takes into account both the temporal correlation of errors in the data time series and the entire variance/co-variance information with the data input. Previous studies have shown that the two sets of velocity solutions of the common sites, are consistent within 0.1 mm/yr and have no obvious systematic deviation. (Wang and Shen, 2020). Therefore, we model the site position time series using equation

((1))(Nikolaidis, 2002) with addition of annual($a \sin(2\pi t_i + \varphi)$) and semiannual($b \sin(4\pi t_i + \varphi)$) variation terms (in sinusoidal form) to obtain the site secular velocity.

Here, we gather all the daily solutions into a single solution in which site position time series is modeled as a function consist of the initial position x_0 at time t_0 , secular velocity V , co-seismic (also instrumental if needed) step C_i , and post-seismic displacement p_i , in the form of

$$x(t) = x_0 + v(t - t_0) + a \sin(2\pi t_i + \varphi) + b \sin(4\pi t_i + \varphi) + \sum_{i=1}^{n_c} c_i H(t - t_i) + \sum_{i=1}^{n_p} p_i H(t - t_i) \ln\left(1 + \frac{t - t_i}{T_i}\right) + r(t_i) \quad (1)$$

where the first summation includes earthquake, instrumental, and other steps at a time t_i , and n_c is the total number of steps; the second summation includes the post-seismic displacements of earthquakes in logarithmic form, t_i and T_i are earthquake occurrence time and decay time constant, respectively, and n_p is the total number of earthquakes. $H(t - t_i)$ is a Heaviside function.

Considering that the only significant earthquakes in Beijing during the period of 1999-2021 is the 2011 Tohoku-Okii M9.0 earthquake, and its post-earthquake effect is only 3-5mm in the recent 25 years, so we does not consider the effect of post-seismic effect, but only consider the effect of co-seismic.

In order to better combine the regional tectonic structure to interpret the obtained result, we transform the velocity solution from ITRF2014 to a relatively stable Eurasia reference frame by using the plate motion model produced by Altamimi et al. (2017) (-0.085,-0.531, and 0.770 mas/yr). The 3-D velocity field with respect to the Eurasian plate is shown in Figure 2. The vertical velocity is plotted as the background and the horizontal velocity is showed with arrow vectors. Vertical velocity appears two distinct subsidence zones in central plain, with about 80 mm/yr at the junction of Haidian, Changping and Chaoyang districts in the north, and up to 130 mm/yr across the Chaoyang and Tongzhou districts. These two regions have a continuous development trend. In addition, the other regions shows slow uplift with about 1-3 mm/yr.

Compared to the vertical velocity, the horizontal velocity is dominated by the SEE direction, which is more consistent with the results obtained by previous studies (Qiao et al., 2008; Wang and Shen, 2020). The overall horizontal velocity is 5-10 mm/yr, with a macroscopic trend of gradually increasing from north to south, and weak variability among internal blocks, reflecting the difference in movement between the Yinshan-Yanshan block and the Jin-Ji-Lu block. Taking the HGF, a north-east fault running through Beijing, as the boundary, the crustal deformation on the east side shows uniform continuous deformation with decreasing rate from west to east, while the west side appears uneven continuous deformation with relatively large differences in overall rate values, which may reflect that the present-day crustal movement in Beijing area is controlled by deep tectonic or mantle material with the destruction of the North China Craton (Zhang et al., 2018).

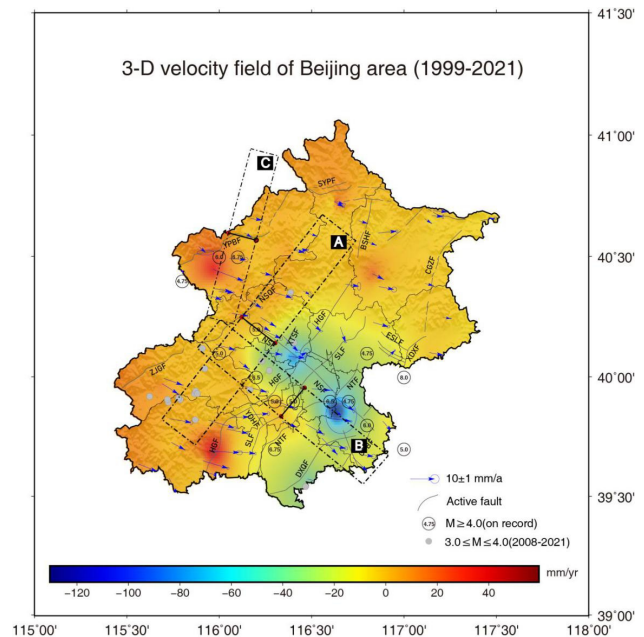


Figure 2. 3-D GNSS velocity field of Beijing area with respect to Eurasian plate.

Blue arrows indicate the GNSS horizontal velocities from this study, and the vertical velocities are plotted at the background. Error ellipses represent 70% confidence. Black dash lines and the alphabet are the GNSS velocity profiles, black solid lines represent the fault relative to the velocity profile, red circle indicated the width of the profile along the fault.

In order to characterize in detail the deformation field in the Beijing area, especially the faults have historically experienced multiple earthquakes of magnitude 4.5 or greater, we make 3 velocity profiles to inspect the regional deformation fields and the main faults activity. We decompose the site velocity into two components: parallel (or along to) and perpendicular (or orthogonal in) to the relative fault, and fit the data parallel to the fault using the arctan function, and plot them in profiles as shown in Figure 3.

In the central of the network (Figure 3a), profiles A, shows crustal motion across the NSF, which shows sinistral shear from its north to south, with slip rates of ~2 mm/yr and accompanied by a slight squeezing motion. At the southeast of Beijing (Figure 3b), there is no significant velocity difference between HGF and SLF, however, after crossing the NTF, the velocity slightly decreases, showing a dextral shear motion of less than 1 mm/yr, which reveals a certain strain accumulation around the NTF. YPBF, located at the northwest boundary of Beijing (Figure 3c), has experienced several earthquakes of M4.5 or higher in history, with a maximum M6.75. YPBF has been significantly active since the Late Pliocene (Zhang et al., 2018), the GNSS velocity profile shows that it has a sinistral shear movement of ~1.1 mm/yr, with weak velocity differences on both sides.

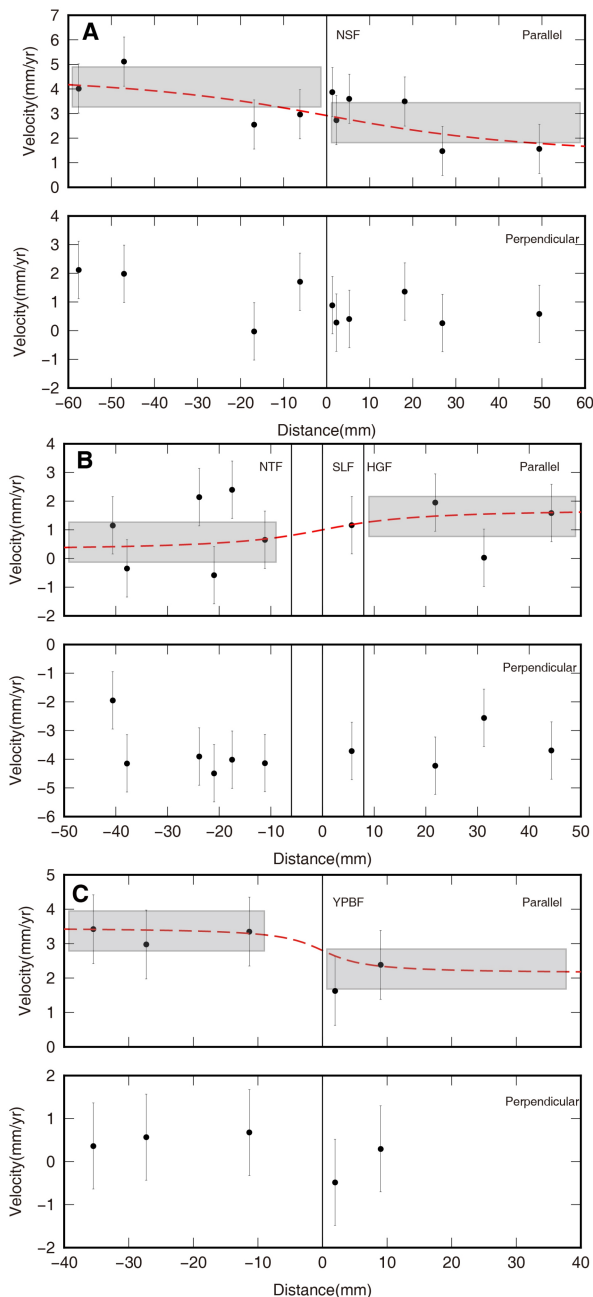


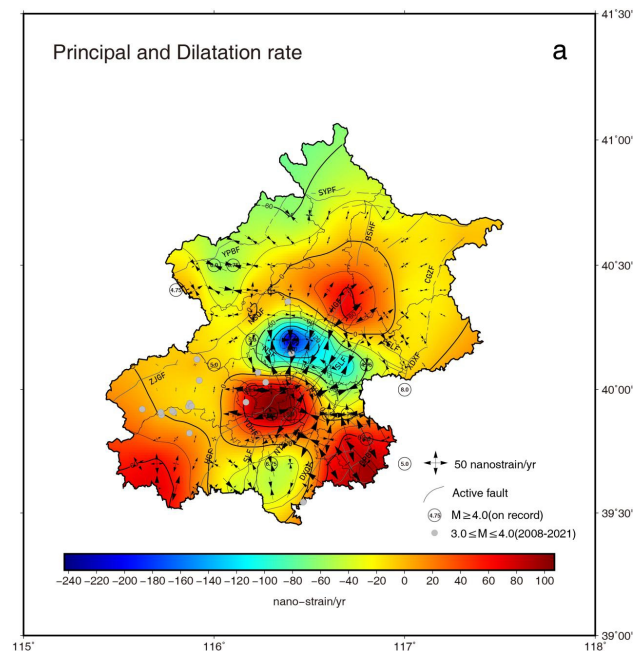
Figure 3. GNSS velocity profiles.

The vertical black solid line shows the fault relative to the velocity profile. Gray box indicates the error range of the fit of arctan function.

3.2 Strain Rate Field

In order to show more clearly the crustal deformation field in Beijing area, we derive a continuum strain rate field by interpolating the horizontal GNSS velocity field using the method developed by Shen et al. (1996, 2015). Considering the discreteness of GNSS velocities, we determine the degree of smoothing which is required for data interpolation, by using the optimal selection of the characteristic distance which is closely related to the spatial density of GNSS sites and the in situ data strength. In this study, 10-20 km is selected as the characteristic distance of the central Beijing area, and 15-25 km is for the north and south area.

The horizontal principal strain rates τ_1 and τ_2 are displayed as conjugate pairs of vectors in Figure 4a, in which the dilatation strain rate $\tau_{dilat} = \tau_1 + \tau_2$ is plotted at the background. It shows that the north-east active faults have a transition gradient zone with tension-compression-tension along the fault strike, up to ~ 220 nanostrain/yr at the north of NSF, which is spatially consistent with the subsidence area of Beijing. The maximum shear strain rates (Figure 4b) τ_{max} demonstrate that the areas between the HGF and the north part of SLF, the middle of NSF and the eastern of YPBF, have strong shear motion of ~ 100 nanostrain/yr, with an inverse 'S'-shaped distribution. At the intersection of NSF and SLF, the maximum shear strain rates show a significant four-quadrant distribution. The rotation rate (Figure 4c) shows that the southwestern and northeastern regions exhibit counterclockwise motion with ~ 20 nanoradian/yr (1.2° /Myr), and up to ~ 110 nanoradian/yr (6.4° /Myr) at the central region. The northwestern and southeastern areas display clockwise motion.



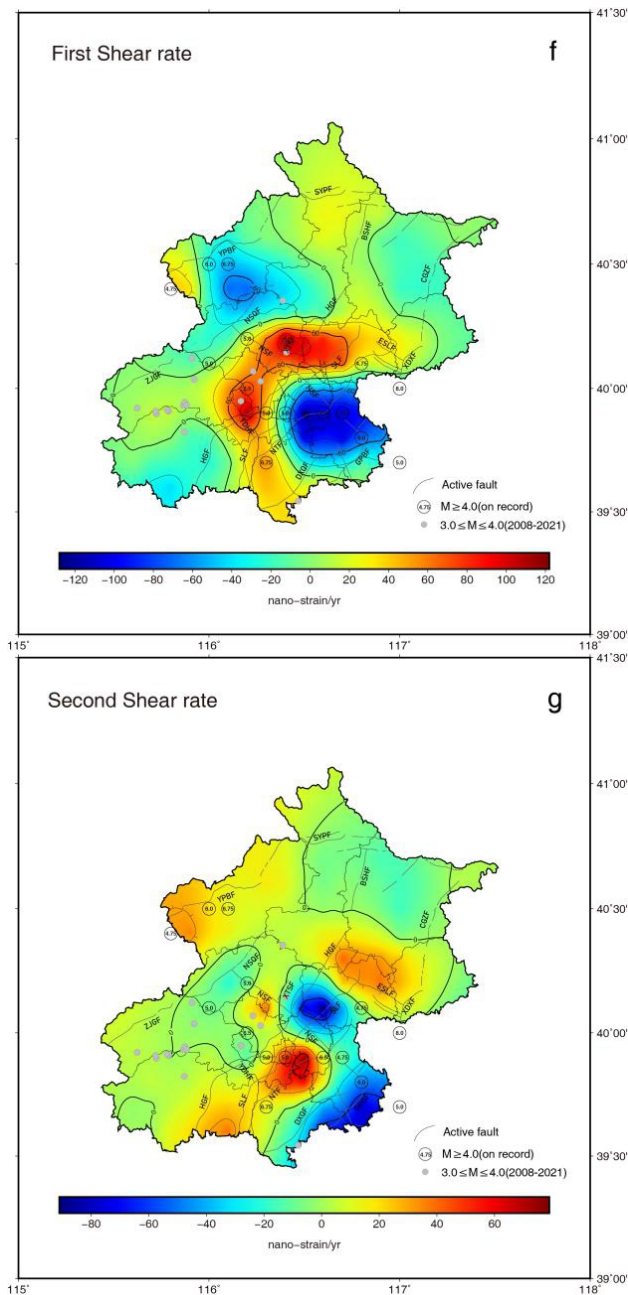


Figure 4. Continuum deformation field of Beijing area derived from interpolation of GNSS velocities.

(a) Strain rates. Dilatation strain rate is shown in background color and principal strain rates are shown as vector pairs. (b) Maximum strain rate. (c) Rotation rate, with counterclockwise rotation positive. (d) East-West rate. (e) North-South rate. (f) First shear strain rate. (g) Second shear strain rate. The gray solid line shows the active faults, and the fault name abbreviations are consistent with those in Figure 1. The gray dots represent the earthquake of M3.0–4.0 occurred between 2008 to 2021. The large hollow circles are the earthquake greater than M4.0 that have occurred on record, the number indicates the magnitude of the earthquake.

To further analyze the strain rate at the north-east and north-west faults in Beijing, we decomposed the strain rate to obtain the east-west (Figure 4d) τ_{ew} and north-south (Figure 4e) τ_{ns} strain rates, the first shear strain rate (Figure 4f) τ_{sh1} , which is

used to characterize the pure shear part of the EW tension and NS compression, the second shear strain rate (Figure 4g) τ_{sh2} , which shows the pure shear part of the NE-SW tension and NW-SE compression. The most of Beijing region is in NS tension and EW extrusion from Figure 4d/e. The east-west strain rate τ_{ew} along the NE faults also show a tension-compression-tension feature, which is spatially consistent with the dilatation rate. This pattern is also seen from north to south on the north-south strain rate τ_{ns} , which also displays the area on both sides of NSF is in strong compression and tension in NS direction, that is, the NSF is in the high gradient zone. The high value of the first shear strain rate and the central area of Beijing subsidence show a ‘vertical mirror’ distribution with a larger range, while the second shear strain rate reflects a ‘scattered’ distribution, but is similar to the maximum shear strain rate at the center of the NSF. These two results both show a significant four-quadrant distribution.

Combined with the historical earthquake distribution, it is found that historical large earthquakes are distributed within the positive and negative gradient zones of the first shear strain rate, and historical large earthquakes are mostly distributed at the edges of the high and low value zones of the second shear strain rate, showing that the edges of the high value zones of the east-west strain rate have a background of large earthquakes, and historical large earthquakes occur in the positive and negative transition zones of the rotation rate.

4. DISCUSSION AND CONCLUSION

In this study we calculate the three-dimensional velocity field of present-day crustal movement, and analyze the deformation and strain characteristics of this region based on more than 100 GNSS sites observation covering the Beijing area, and also examine the regional main active faults accompanied by historical earthquakes. Our conclusions shows below:

1. Compared with the stable Eurasian plate, the present-day crustal horizontal movement in the Beijing area is dominated by the SEE direction, with a rate of 5-10 mm/a. Overall, it shows a certain consistency, with a macroscopic trend of gradual increase from north to south, and weak variability among the internal blocks, reflecting the difference in movement between the Yinshan-Yanshan block and the Jin-Ji-Lu block. Taking the HGF, a north-east fault running through Beijing, as the boundary, the crustal deformation on the east side shows uniform continuous deformation with decreasing rate from west to east, while the west side appears uneven continuous deformation with relatively large differences in overall rate values, which may reflect that the present-day crustal movement in Beijing area is controlled by deep tectonic or mantle material with the destruction of the North China Craton.

2. The vertical velocity shows differential uplift and subsidence movements, with about 1-3 mm/a uplift in the northern and southern areas, and the central plain exhibits an overall subsidence and shows two distinct subsidence zones at the intersection of Haidian, Changping and Chaoyang districts in the north with about 80 mm/yr, and up to 130 mm/yr across the Chaoyang and Tongzhou districts. These two regions have a continuous development trend. The distribution of subsidence areas is consistent with the spreading direction of regional faults on a macroscopic scale, showing a bidirectional spreading in the N-W and N-E directions, which indicates a significant

correlation between the distribution of present-day vertical crustal motion and regional faults in Beijing.

3. The horizontal deformation is mainly NE and NW extension, accompanied by weak shear activity. The N-W trending faults show sinistral strike slip movement as a whole, with about 1.1-2.0 mm/a, and NE trending faults show dextral strike slip with a rate of less than 1 mm/a.

4. The active faults spreading in the NE direction have a tension-extrusion-tension intersection gradient zone along the fault direction, and the strong compression zone is located in the north side of the NSF, with a maximum compression rate of about 220 nanostrain/yr, which spatially coincides more with the subsidence region in Beijing, and the region has significant variability on both sides of the NSF with NW-trending. The strong shear region is located in the area between the HGF, the northern section of the SLF, the middle section of the NTF fault and the eastern area of the GPBF, which spatially shows an inverse "S"-shaped distribution with a significant four-quadrant distribution at the intersection of the NSF and the SLF.

ACKNOWLEDGEMENTS

We are very grateful to all the contributors to GAMIT/GLOBK software. GAMIT/GLOBK is available as a free download of authorization (<http://geoweb.mit.edu/>). Thanks very much for all the contributors of the Crustal Movement Observation Network of China I and II (CMONOC-I/II). This work is supported by the Beijing Natural Science Foundation, China (8204077) and the National Natural Science Foundation of China (42004010).

REFERENCES

Altamimi Z., Métivier L., Rebischung P., et al.. ITRF2014 plate motion model[J]. *Geophysical Journal International*. 2017,209(3).1906–1912.

Boehm J., Heinkelmann R. Schuh H. Short note: a global model of pressure and temperature for geodetic applications[J]. *Journal of Geodesy*,2007, 81, 679-683.

Boehm J., Werl B., Schuh H. Troposphere mapping functions for GPS and very long baseline interferometry from European Centre for Medium-Range Weather Forecasts operational analysis data[J]. *Journal of Geophysical Research: Solid Earth* 2006, (1978–2012), 111.

Gao M. T. GB18306-2015 "Seismic ground motion parameter zonation map of China" publicity and implementation materials [M]. *China Quality Inspection press*, 2015.

Gao W. X. and Ma J. Seismogeological environment and earthquake disasters in the capital circle [M], *Beijing: Seismological Press*, 1993,30-45.

Guo L. Q., Ma Q., Yang G. H. Modern movement and strain of main tectonic zones in North China [J] *International earthquake dynamics*, 2007 (7): 9.

Herring T. A., King R. W., McClusky S. C. . GAMIT reference manual, GPS Analysis at MIT, Release 10.4. *Cambridge, MA:Massachusetts Institute of Technology*. 2010a.

Herring, T. A., King, R. W., McClusky, S. C. . GAMIT reference manual, Global Kalman filter VLBI and GPS analysis

program,Release 10.4. *Cambridge, MA: Massachusetts Institute of Technology*.2010b.

Jiang Z. S., Ma Z. J., Zhang X., et al. The horizontal strain field and tectonic deformation of Chinese Mainland revealed by preliminary GPS results [J] *Journal of Geophysics*, 2003, 46 (3): 352-358.

Jiang Z. S., Wu Y. Q. Crustal deformation and prediction of strong earthquake sites [J] *Earthquake*, 2012, 32 (2): 8-21.

Lagler K., Schindelegger M., Bohm J. et al. GPT2: Empirical slant delay model for radio space geodetic techniques[J]. *Geophysical Research Letters*, 2013, 40(6):1069-1073.

Li Y. The impact on the Northeast and North China caused by the Tohoku-Oki Earthquake in Japan in 2011[D]. *Institute of Geology, China Earthquake Administration*.2013.

Li, Y. Analysis of GAMIT/GLOBK in high-precision GNSS data processing for crustal deformation, *Earthquake Research Advances*, 2021, 1(3):29-37.

Lyard F., Lefevre F., Letellier T. et al. Modeling the global ocean tides: Modern insights from FES2004. *Ocean Dynamics*,2006,56, 394–415.

Ma Z. J. Study on geological structure of Yanshan District -- a brief account of the two reports of Beijing Geological Society[J]. *Geological review*, 1964, 22 (2): 163-164.

Macmillan S. and Maus S. International Geomagnetic Reference Field—the tenth generation[J], *Earth Planets Space*, 2005, 57, 1135–1140.

Maus S., Macmillan S., Lowes F., et al. Evaluation of candidate geomagnetic field models for the 10th generation of IGRF[J], *Earth Planets Space*, 57, 1173–1181, 2005b.

Nikolaïdis R. Observation of geodetic and seismic deformation with the Global Positioning System[D]. *University of California, San Diego*, 2002,249.

Qiao X. J., Chen Y., Wang Q., et al. GPS observation and tectonic activity simulation of current crustal movement in the capital circle area [J] *Journal of Wuhan University: Information Science Edition*, 2008, 33 (7): 5.

Ran Y. K., Deng Q. D., Yang X. P., et al. Paleo earthquakes on the seismogenic fault of the 1679 Sanhe Pinggu Ms8 earthquake and their recurrence intervals [J] *Seismogeology*, 1997,19 (3).

Ren Z. Q. Historical earthquakes in Beijing area [J] *International earthquake dynamics*, 1996 (9): 34-35.

Saastamoinen, J.. Contributions to the theory of atmospheric refraction. *Bulletin Géodésique*, 1973,107, 13-34.

Shen Z. K., Jackson D. D. Bob X. G. Crustal deformation across and beyond the Los Angeles basin from geodetic measurements[J]. *Journal of Geophysical Research: Solid Earth*, 1996(101), 27957-27927.

Shen Z. K., King R. W., Agnew D. C., et al. A unified analysis of crustal motion in Southern California, 1970-2004: The SCEC crustal motion map. *Journal of Geophysical Research: Solid Earth*, 2011(116), B11402.

Shen Z. K., Wang M., Zeng, Y. et al. Optimal interpolation of spatially discretized geodetic data[J]. *Bulletin of the Seismological Society of America*, 2015,105(4), 2117–2127.

Wang M., Shen Z. K. Present-Day Crustal Deformation of Continental China Derived From GPS and Its Tectonic Implications[J]. *Journal of Geophysical Research: Solid Earth*, 2020, 125(2).

Xu X. W., Wu W. M., Zhang X. K, et al. The latest tectonic changes and earthquakes in the capital region [M] *Beijing: Science Press*, 2002.

Yang G. H., Wang M., Han Y. P. Crustal movement in North Central China and Zhangbei earthquake [J]. *China earthquake*, 2001, 17 (3): 304-311.

Zhang Y. G., Zheng W. J., Wang Y. J., et al. Contemporary Deformation of the North China Plain From Global Positioning System Data[J]. *Geophysical Research Letters*, 2018, 45(4).